Barsk, Aleksi; Yazdani, Maryam Roza; Kankkunen, Ari; Seppälä, Ari

Exceptionally high energy storage density for seasonal thermochemical energy storage by encapsulation of calcium chloride into hydrophobic nanosilica capsules

Published in:
Solar Energy Materials and Solar Cells

DOI:
10.1016/j.solmat.2022.112154

Published: 01/03/2023

Document Version
Publisher's PDF, also known as Version of record

Please cite the original version:
Barsk, A., Yazdani, M. R., Kankkunen, A., & Seppälä, A. (2023). Exceptionally high energy storage density for seasonal thermochemical energy storage by encapsulation of calcium chloride into hydrophobic nanosilica capsules. *Solar Energy Materials and Solar Cells*, *251*, Article 112154.
https://doi.org/10.1016/j.solmat.2022.112154

Solar Energy Materials & Solar Cells 251 (2023) 112154

Contents lists available at ScienceDirect

Solar Energy Materials and Solar Cells

journal homepage: www.elsevier.com/locate/solmat

Exceptionally high energy storage density for seasonal thermochemical energy storage by encapsulation of calcium chloride into hydrophobic nanosilica capsules

Aleksi Barsk, Maryam Roza Yazdani, Ari Kankkunen, Ari Seppälä *

Aalto University School of Engineering, Department of Mechanical Engineering, Energy Conversion, P.O. Box 14400, FI-00076, Aalto, Finland

ARTICLE INFO

Keywords:
Thermochemical energy storage
Sorption properties
Deliquescence
Fumed silica
$CaCl_2$
Energy storage density
Phase inversion

ABSTRACT

Thermochemical energy storage (TCES) in salt hydrates is a promising method for seasonal thermal energy storage. However, salt hydrates suffer from agglomeration and deliquescence drastically degrading their performance after just a few cycles. Here, modified dry water-style preparation methods are developed for leakage-free microencapsulation of $CaCl_2$ with hydrophobic fumed silica nanoparticles. Using a novel phase inversion method, as little as 2 wt% of silica is needed for complete encapsulation, ensuring exceptionally high gravimetric energy storage densities up to 98% of pure $CaCl_2$. With temperature lifts of 30 °C, volumetric energy storage densities up to 1.4 GJ/m^3 are shown to be achievable. These values are unprecedented for cycle-stable sorption TCES materials.

Optical microscopy, scanning electron microscopy and laser diffraction analysis confirm the encapsulation of $CaCl_2$ into capsules with volume median diameters ranging from 90 to 210 μm depending on silica content and preparation method. The encapsulated $CaCl_2$ deliquesces with lower water vapor pressures than pure $CaCl_2$ and no formation of tetrahydrate and hexahydrate is observed. Despite deliquescence, the encapsulated $CaCl_2$ is completely stable for at least 30 cycles of charge-discharge. Thus, the new materials show excellent potential for seasonal thermal energy storage.

1. Introduction

Solar heat is available in large amounts during summer. However, to utilize it for heating in the winter when the demand is high, effective means of storing heat for months without exceedingly large thermal losses are needed [1]. Thermochemical energy storage (TCES) via the sorption of water into hygroscopic salts offers both high energy storage density and very low losses in long-term heat storage [2,3]. In sorption TCES, during charging phase, water bonded with the salt either in solid state as a salt hydrate or in liquid solution is evaporated by heating the salt hydrate or solution to a higher temperature [3]. This dehydration is a highly endothermic reaction [3]. During storage period the charged material is kept separated from water. When heating output is needed (discharging), water vapor, often in the form of humid air, is brought in contact with the salt or concentrated salt solution, leading to a highly exothermic hydration reaction and thus, an increase in temperature [3].

Many salt hydrates could in theory achieve high volumetric energy storage densities (*VSD*) of close to or even over 2 GJ/m^3 [4]. This makes them suitable e.g., for seasonal thermal energy storage for residential building space heating, with the charging heat provided during summer by solar heat collectors. However, despite the impressive theoretical energy storage densities of many salt hydrates, their application in large scale systems has faced significant issues due to e.g., material degradation [5] and even *VSD* of 1 GJ/m^3 has shown to be difficult to achieve [6]. Especially deliquescence can cause large problems in terms of reversibility of the hydration reaction. Deliquescence is a phenomenon where, if relative humidity (RH) exceeds the deliquescence relative humidity (DRH), the solid salt transitions into a liquid solution [3]. Even the formation of a thin liquid layer on salt particle surfaces during sorption can lead to significant agglomeration upon subsequent solidification [7] while complete dissolution eliminates all surface area required for the sorption reactions. Thus, even partial deliquescence is often highly detrimental to the system performance. In addition, partial or complete melting of the higher salt hydrates can occur if, during heating, the higher hydrates melting point is achieved before dehydration to a lower level is completed [8]. This can also lead to agglomeration.

---

* Corresponding author.
E-mail address: ari.seppala@aalto.fi (A. Seppälä).

https://doi.org/10.1016/j.solmat.2022.112154
Received 12 July 2022; Received in revised form 3 November 2022; Accepted 12 December 2022

Abbreviations

BET	Brunauer–Emmett–Teller
dir	direct mixing method
DRH	deliquescence relative humidity
EDX	energy-dispersive X-ray spectroscopy
inv	phase inversion method
RH	relative humidity
SEM	scanning electron microscopy
SiO_2	silica, silicon dioxide
STA	simultaneous thermal analysis
TCES	thermochemical energy storage

Symbols

$D_{V,0.5}$	volume median diameter (m)
$D_{V,0.9}$	particle size below which 90% of the volume distribution is located (m)
ER	encapsulation ratio (dimensionless)
GSD	gravimetric energy storage density, dry basis (J/kg)
GSD_{wet}	gravimetric energy storage density, wet basis (J/kg)
m_{dry}	mass after drying (kg)
m_{eq}	mass in equilibrium with the surrounding water vapor (kg)
m_{h_i}	mass after hydration cycle i (kg)
m_{SiO2}	mass of fumed silica (kg)
m_{CaCl_2}	mass of anhydrous $CaCl_2$ (kg)
m_{H_2O}	mass of water (kg)
m_{EtOH}	mass of ethanol (kg)
M_{CaCl_2}	molar mass of calcium chloride (kg/mol)
M_{H_2O}	molar mass of water (kg/mol)
n	hydration level (dimensionless)
n_{eq}	hydration level when material is in equilibrium with water vapor (dimensionless)
p_{H_2O}	water vapor pressure (Pa)
SR	sorption ratio (dimensionless)
T_d	dew point (°C)
T_h	hydration temperature (°C)
T_{prep}	preparation temperature (°C)
q	released heat per unit mass (J/g)
$q_{encap,CaCl_2}$	released heat per unit mass of capsules of $CaCl_2$ (J/g)
q_{CaCl_2}	released heat per unit mass of $CaCl_2$ (J/g)
V_{EtOH}	volume of ethanol (m^3)
VSD	volumetric energy storage density (J/m^3)
w	equilibrium water intake (dimensionless)
y	fumed silica mass fraction, dry basis (dimensionless)
x	fumed silica mass fraction, wet basis (dimensionless)

Greek symbols

α_i	relative water intake for cycle i (dimensionless)
ΔH	enthalpy change of reaction (J/mol)
$\Delta_{dil} H$	enthalpy change of dilution (J/mol)
$\Delta_{con} H$	enthalpy change of condensation (J/mol)
$\Delta_m H_{CaCl_2 \cdot 6\ H_2O}$	enthalpy change of melting of the hexahydrate (J/mol)
$\Delta_r H_{CaCl_2 \cdot n\ H_2O}$	enthalpy change for hydration from anhydrous state to solid hydrate with n H_2O molecules (J/mol)
ξ	solution mass fraction (dimensionless)
$\xi_{6\ H_2O}$	solution mass fraction of $CaCl_2$ hexahydrate melt (dimensionless)
ξ_{eq}	solution mass fraction when in equilibrium with water vapor (dimensionless)
ρ_{aq}	density of aqueous solution (kg/m^3)
$\rho_{aq,eq}$	density of $CaCl_2$ solution inside the capsules in equilibrium with water vapor (kg/m^3)
ρ_{bulk}	bulk density (kg/m^3)
$\rho_{capsule}$	average capsule solid density (kg/m^3)
ρ_{EtOH}	ethanol density (kg/m^3)
ρ_{SiO2}	fumed silica solid density (kg/m^3)
φ_{liq}	liquid volume fraction (dimensionless)
$\varphi_{SiO_2,caps}$	average volume fraction of SiO_2 in the capsules (dimensionless)
φ_V	void fraction (dimensionless)

Numerous attempts have been made to reduce agglomeration e.g., by infusing salts into different solid adsorbents such as silica gel and zeolite as well as non-reactive porous host matrices such as vermiculite and expanded graphite [5,9,10]. Recently, microencapsulation of salt hydrates into porous shells has also gained interest with materials such as hydrophobic polymers [11,12] and hydrophilic hollow silica [6,12] tested. However, in many of the methods used, the amount of material needed for elimination of agglomeration is rather high. Thus, the gravimetric and especially the volumetric energy storage density of the system suffers with *VSD* usually dropping below 1 GJ/m^3 [6]. Thus, the viability of the salt composite as an effective energy storage medium is reduced. New methods that reduce agglomeration with minimal use of non-reactive material are still needed for salt sorption to become a viable option for thermal energy storage.

So-called “dry water” consist of small, stable nanoparticle-encapsulated water droplets that behave like a free-flowing powder [13]. This concept can be used to encapsulate aqueous salt solutions as well [14]. Dry water is formed when hydrophobically surface-treated fumed silica is mixed with water in a high-speed blender directly or with lower speed mixing after atomization [15]. During the preparation of dry water, small water droplets form which are quickly surrounded by the hydrophobic nanoparticles that attach to the surface due to surface energies, trapping the water inside and resulting in a water-in-air “emulsion” [16]. The result is a powder-like, free-flowing substance, that can be up to 98% water [15]. Water cannot escape these capsules without mechanical stress, except via evaporation [13,15,17].

Recently, dry water has gained interest and the concept has been used e.g., to encapsulate K_2CO_3 for CO_2 capture [14,18–20]. A patent from 2012 [21] also describes the encapsulation of different salts and CaO with hydrophobic silica nanoparticles and the use of such compositions for e.g., sorption TCES. However, no detailed data or scientific publications are available concerning the performance of such nano-encapsulated salts in sorption TCES. Additionally, prior reports of salt encapsulation with the dry water concept describe encapsulation only with high silica contents of over 10 wt% on dry salt basis. Due to the highly branched structure and resulting extremely low density of fumed silica, the overall density of dry water style-materials tends to drop drastically as silica content is increased [13].

In this study, we develop two novel modified dry water-style preparation methods for encapsulation of $CaCl_2$ with as little as 2 wt% SiO_2 nanoparticles in the resulting composition. We study the properties of such nanoparticle-encapsulated salts with emphasis on their performance as sorption TCES under repeated charge-discharge cycles, the achievable energy storage densities, reaction kinetics and the effect of preparation method on these properties.

2. Materials and methods

2.1. Materials

Highly hydrophobic fumed silica particles (Aerosil R812S) were supplied by Evonik Industries AG. Its properties are listed in Table 1.

Table 1
Aerosil R812S properties. Data from [22] is by the manufacturer.

Physical property	Aerosil R812S	Refs
Specific surface area (BET)	195-245 m^2/g	[22]
Mean primary particle size[a]	9–12 nm	[22]
Average aggregate size[b]	270 nm	[15]
Water contact angle[c]	118°	[16]
Tamped density	60 g/l	[22]
Carbon content	3–4%	[22]
Substituting group	Hexamethyldisilazane	[22]
Loss on drying	<0.5%	[22]

[a] Approximated based on relation between specific surface area and primary particle size presented in [22].

[b] After 10 min of ultrasonic dispersion in ethanol.

[c] Measured with water intrusion method.

Calcium chloride dihydrate (ACS Reagent grade, $\geq$ 99%) and lithium chloride ($\geq$ 99.98% trace metal basis) were purchased from Sigma-Aldrich. Ethanol (Etax Aa, $\geq$ 99.5%) was purchased from VWR. Deionized water was used in all preparations.

Fumed silica consists of sintered branched networks, called aggregates, of primary amorphous silica (SiO_2) spheres of typical size 10–20 nm that are manufactured in a combustion process [15]. This aggregate structure, briefly illustrated in Supplementary Fig. S1, causes the exceptionally low density of fumed silica [22]. These aggregates, which can have sizes up to several hundred nm, are formed by the collision and fusion of primary silica spheres at high temperatures. Upon cooling, larger weakly bonded agglomerates of 20–30 μm size can form via mechanical entanglements or van der Waals forces, but these can easily be broken e.g., via sonication [15]. However, the sintered aggregates usually remain intact as they have much higher energy O–Si–O bonds between them. In Aerosil R812S, the fumed silica aggregates have been further surface-treated with hexamethyldisilazane to make them hydrophobic.

2.2. Preparation of encapsulated $CaCl_2$

A high speed-blender Bosch SilentMixx model MMB66G7M with a $\sim$400 ml closed plastic container was used to mix the $CaCl_2$ solutions with the silica nanoparticles. The blender rotation speed was measured with a handheld Monarch Pocket-Tach Plus to be around 7000 rpm at full power. Two different preparation methods (Fig. 1) were used. Both methods include mixing a small amount of ethanol into the $CaCl_2$ solution before the high-speed mixing. We found that this was required for the creation of low SiO_2 mass fraction composites with complete encapsulation. The compositions prepared are shown in Table 2.

In method one, referred to as direct mixing method (dir), 0.9 ml of ethanol was first mixed with $\sim$50 g of 43 wt% $CaCl_2$ solution in the blender container at room temperature before pouring in varying amounts of fumed silica. The blender was then used at full power for 30 s. The container was then turned upside down and lightly shaken by hand for a few seconds after which the sample was mixed with the blender for another 30 s at full power.

Table 2
Prepared compositions. Number in the name gives the SiO_2 wt% of dried sample. inv refers to samples made with the phase inversion method while dir refers to samples made with the direct mixing method. ξ is the mass fraction of $CaCl_2$ in the solution before ethanol addition. V_{EtOH} is the amount of ethanol added during preparation. T_{prep} refers to the approximate temperature of the solution and fumed silica during preparation.

Composition	ξ	Solution mass (g)	V_{EtOH} (ml)	T_{prep} (°C)
inv-2.0	0.56	54.3	1.1	$\sim$ 65
inv-2.5	0.43	50.0	1.2	$\sim$ 25
inv-4.9	0.43	50.0	1.5	$\sim$ 25
dir-4.9	0.43	50.0	0.9	$\sim$ 25
inv-7.2	0.43	50.0	1.7	$\sim$ 25
dir-7.2	0.43	50.0	0.9	$\sim$ 25

While the direct mixing method functions well for silica contents of $\sim$5 wt% or more (on dry salt basis), complete encapsulation was not achieved if very low amounts of silica were used. In method two, referred to as the phase inversion method (inv), a slightly higher amount of ethanol (see Table 2) was added to the $CaCl_2$ solution (43 wt% or 56 wt%) before adding the fumed silica. If a 43 wt% solution was used, the preparation was done at room temperature but for 56 wt% solution, the solution, container, blender blade and the fumed silica were pre-heated together to $\sim$65 °C. In both cases, sample was then mixed at full power in the blender for 30 s which led to a formation of a continuous white substance (Fig. 1, middle). The precise structure of this phase is uncertain. The continuous structure would indicate that the structure is an air-in-water foam with air bubbles encapsulated by the nanoparticles. However, small pieces could be cut from the structure. These cut pieces bear resemblance to the soufflé-like material described by Binks and Murakami [13] as they did not stick to surfaces and or easily disperse in $CaCl_2$ solution. The structure may also be of water-in-air-in-water type described by Binks et al. [23]. The precise structure should be studied later but for simplicity, in this study we will refer to this phase as foam.

After forming the foam, the container was turned upside down and strongly shaken by hand until the sample had changed into a white powder-like substance, i.e., the sample had gone through phase inversion. The time required for phase inversion to occur varied from sample to sample but was generally less than 30 s. The sample was then further mixed for another 30 s in the blender which led to foam forming again and then the mixture was phase inverted again through handshaking.

Note that the sample mass used was slightly higher for the 56 wt% solution to keep the volume of sample approximately constant as the higher mass fraction solution has an increased density. Thus, the volume fraction of the water phase relative to air, a parameter that has been

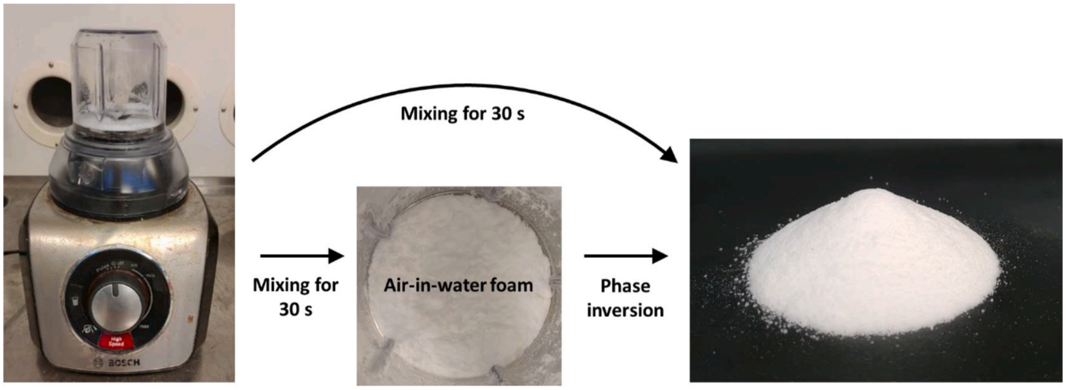

Fig. 1. Preparation methods of silica encapsulated $CaCl_2$.

found to affect dry water formation [13], was kept near constant between different compositions.

The precise amounts of materials used for each composition are listed in Table 2. The SiO_2 content of dried sample used for naming the samples was determined as $y = \frac{m_{SiO2}}{m_{SiO2}+m_{CaCl_2}}$, where m_{CaCl_2} is the mass of anhydrous $CaCl_2$ in the encapsulated solution and m_{SiO2} is the mass of fumed silica used.

Note that in Table 2, ξ refers to mass fraction of $CaCl_2$ in the solution before addition of ethanol. Thus, the mass fraction of solution during encapsulation varies slightly between the compositions where 43 wt% $CaCl_2$ was used, as differing amounts of ethanol was added. For each composition, two batches were made to ensure the preparation methods were repeatable.

The preparation methods were quite sensitive to the amount of ethanol added. Small amounts of ethanol led to incomplete encapsulation when the direct mixing method was used whereas excessive amounts of ethanol led to irreversible foam formation, i.e., handshaking could no longer induce phase inversion. Irreversible phase inversion upon addition of a surfactant is known to occur for dry water (Binks et al., 2009), but the subsequent phase inversion back to water-in-air powder upon hand shaking seems to be a novel feature that has not, to our knowledge, been reported yet. While only $CaCl_2$ was encapsulated in this study, we expect the preparation methods to work on other salts as well.

2.3. *Morphological characterization*

Polarized optical microscope (Leica DM4500) was used to take images of the samples at room temperature. Scanning electron microscopy (SEM) was performed on a Zeiss Sigma VP microscope and a JEOL JSM-7500FA analytical field emission scanning electron microscope under vacuum and at 2–4 kV acceleration voltage. The powder samples were first attached on a metal stub with carbon tape and coated with a 4 nm layer of gold palladium alloy in a Leica EM ACE600 sputter coater prior to the SEM. Energy-dispersive X-ray spectroscopy (EDX) was also conducted at 15.0 kV acceleration voltage to detect the elemental composition of the capsules surface. No coating was used for this measurement.

Brunauer–Emmett–Teller (BET) surface area analysis was conducted on a Microtrac BELsorp Mini II. The pore size distribution was determined via the Dollimore-Heal (DH) method. Prior to the BET measurement, the powder samples were dried overnight and put in a Microtrac BELPrep Vac II Pre-Treatment Station for degasification under 150 °C for 2 h with flowing nitrogen gas.

X-ray diffraction (XRD) was carried out on the powder samples using a Rigaku SmartLab X-ray diffractometer with a rotating anode X-ray source (9 kW, Cu Kα1) and a HyPix-3000 2D detector.

Laser diffraction measurements were carried out with Malvern 2600 Mastersizer. Dried samples were dispersed in kerosene in a 12.5 ml cuvette with continuous mixing using a magnetic stirrer to prevent particles from instantly falling to the bottom. The volume concentrations determined by the Mastersizer software varied from 0.01 vol% to 0.05 vol% for different measurements. As larger particles still tended to sediment, measurements were started after just a few seconds of mixing. 2000 sweeps were used for the measurement so that the total measuring time was around 15 s. Malvern's model independent droplet size distribution model was used to determine the particle size distributions, volume median diameters ($D_{V,0.5}$) and 90th percentiles ($D_{V,0.9}$), i.e., particle sizes below which 90% of the volume distribution is located.

2.4. *Thermal conductivity*

Thermal conductivity was measured with CTherm TCi analyzer. Before the tests, the analyzer was calibrated with distilled water, expanded polystyrene, LAF foam, PVC and Pyrex.

From each composition three wet and three dry ~1.8 ml samples were analyzed. Here wet samples refer to samples taken in the condition they were after preparation while dry samples were dried overnight in an oven at 200 °C.

2.5. *Determination of sorption properties*

The ability of the encapsulated salts to absorb water and release heat during a cycle of dehydration and subsequent rehydration was studied with simultaneous thermal analysis (STA) apparatus (Netzsch STA 449 F3 Jupiter) connected to a modular humidity generator (ProUmid MHG32) and equipped with a vortex tube cooler. The humidity generator was calibrated with pure LiCl using the correlation between mass fraction and water vapor pressure presented in [24]. Possible inaccuracy in equilibrium mass change measurements was estimated to be less than 1% and it mainly comes from inconsistency of the humidifier and baseline drift over long measurements.

For measuring sorption enthalpies and equilibrium water content, sample with mass ranging from 6 to 12 mg was placed in an open 25 μl aluminum crucible in the STA measurement chamber and heated to 150 °C at a rate of 10 K/min and kept there for 60 min. Then the sample was cooled to the desired temperature and once temperature had stabilized, the humidity generator was switched on to generate humid nitrogen flow at a rate of 150 ml/min for the isothermal hydration step which was continued until sample mass had stabilized. For comparison, pure $CaCl_2$ was also studied in STA with the same program. It was used as such without any grinding. During the experiments, purge and protective gas flows were set to 20 ml/min.

The measured weight gain was used to determine the equilibrium water intake w in g-H_2O per 1 g of dried sample $w = \frac{m_{eq}-m_{dry}}{m_{dry}}$, where m_{eq} is the sample mass in equilibrium with the surrounding water vapor and m_{dry} is the sample mass after drying at 150 °C. Sorption ratio was determined as $SR = \frac{w_{encap,CaCl_2}}{w_{CaCl_2}}$, where $w_{encap,CaCl_2}$ and w_{CaCl_2} are the equilibrium water intakes for the composite samples and pure $CaCl_2$ respectively. Hydration level was determined as

$$n = \frac{\frac{m_{eq}-m_{dry}}{M_{H_2O}}}{\frac{m_{dry}(1-y)}{M_{CaCl_2}}} \tag{1}$$

where M_{H_2O} and M_{CaCl_2} are the molar masses of water and $CaCl_2$ respectively. Based on measured reaction heats in STA, encapsulation ratio was determined as $ER = \frac{q_{encap,CaCl_2}}{q_{CaCl_2}}$, where $q_{encap,CaCl_2}$ and q_{CaCl_2} are the measured releases of heat per unit mass of the encapsulated and pure $CaCl_2$ samples respectively.

It has been previously observed by Gaeini et al. [11] that reaction heats of the salt hydration reactions can be underestimated by STA measurements by up to 15–30% due to e.g., higher thermal losses to surrounding gas phase in the relatively slow hydration reactions compared to much faster metal melting reactions used for calibration of STA. Furthermore, the STA device we used was only calibrated by melting samples at constant heating rates whereas the sorption reaction took place under isothermal conditions. Thus, to get more accurate estimates for gravimetric energy storage density (*GSD*) of different compositions, reaction enthalpy of pure $CaCl_2$ was first determined based on equilibrium hydration level as

$$\Delta H = \Delta_r H_{CaCl_2\cdot 6\ H_2O} + \Delta_m H_{CaCl_2\cdot 6\ H_2O} + \Delta_{dil} H\left(\xi_{6\ H_2O} \rightarrow \xi_{eq}\right) + \Delta_{con} H\cdot\left(n_{eq} - 6\right) \tag{2}$$

where $\Delta_r H_{CaCl_2\cdot 6\ H_2O}$ is reaction enthalpy for hydration from anhydrous state to hexahydrate, $\Delta_m H_{CaCl_2\cdot 6\ H_2O}$ is the melting enthalpy of the hexahydrate while $\Delta_{dil} H(\xi_{6\ H_2O} \rightarrow \xi_{eq})$ and $\Delta_{con} H\cdot(n_{eq} - 6)$ are the dilution enthalpy and the condensation heat of water vapor from hexahydrate state, where $n = 6$, to equilibrium conditions at which hydration level is n_{eq}, respectively. All reaction enthalpies are on molar basis, i.e. in units

$\frac{\mathrm{kJ}}{\mathrm{mol}_{\mathrm{CaCl}_2}}$ except $\Delta_{con}H$ which is in units $\frac{\mathrm{kJ}}{\mathrm{mol}_{\mathrm{H}_2O}}$. A more detailed description of Eq. (2) is given in Supplementary information. The relevant thermodynamics properties are from [24–27]. *GSD* of different compositions and pure $CaCl_2$ was then calculated as

$$GSD = SR\frac{\Delta H}{M_{CaCl_2}} \tag{3}$$

To evaluate an isotherm of water intake under different vapor pressures at 30 °C, the sample was dehydrated at 150 °C and then cooled to 30 °C. Once stable temperature was achieved, water vapor pressure was increased stepwise, and the sample was allowed to reach equilibrium conditions for each step while changes in mass were recorded. For these experiments small samples of inv-2.0 containing 1–2 mg of dry $CaCl_2$ were used.

The rehydration kinetics were evaluated with the same temperature program as the sorption equilibrium properties. Since sample masses are known to affect reaction kinetics quite significantly, for these measurements the samples were weighted so that there was approximately 5 mg of dry $CaCl_2$ in each sample.

For dehydration kinetics evaluation, another heating step was added to heat the sample to 200 °C at 10 K/min after equilibrium was achieved during absorption at 30 °C with water vapor pressure set to $p_{H_2O} = 1.3$ kPa. At the start of the heating step, water vapor supply was cut off and purge gas flow was increased to 100 ml/min to decrease water vapor build-up in the STA chamber.

Dehydration kinetics were also evaluated in isothermal conditions with the following program: First samples with ~5 mg of $CaCl_2$ were dried by heating to 100 °C under pure nitrogen flow. Then, the samples were cooled down to 80 °C and subsequently hydrated to solid dihydrate state by setting the water vapor pressure to 4 kPa. Finally, humidity was set to zero and the samples were allowed to dry again. Based on the thermogravimetric data, hydration level n was then determined as a function of time with $t = 0$ set as the moment the humidity was set to zero.

2.6. *Cycling stability*

Cycling stability was tested in STA by running a temperature program that consisted of a heating step at 10 K/min to 120 °C, an isothermal segment at 120 °C for 30 min, cooling down at ~3 K/min to 30 °C and an isothermal segment at 30 °C for around 2.5 h. This cycle was repeated 10 times for all compositions. In addition, for inv-2.0, an experiment with 30 cycles with the same temperature program was performed. Water vapor pressure was kept at ~1.5 kPa with a flow rate of 150 ml/min to ensure that the samples hydrated to a completely liquid state during the rehydration steps. For the cycling experiments, relative water intake was defined as $\alpha_i = \frac{m_{h_i} - m_{dry}}{m_{h_1} - m_{dry}}$, where m_{h_1} and m_{h_i} are the masses of the sample at the end of the hydration steps of cycle one and i respectively.

2.7. *Energy storage density*

Based on known relationships between water vapor pressure and $CaCl_2$ hydration level at different temperatures taken from [24,28], ΔH was predicted at different hydration conditions. The method is covered in more detail in Supplementary information, but briefly, Eq. (2) was used for liquid states while for solid hydrate states, ΔH was determined simply as the reaction enthalpy of hydration from anhydrous $CaCl_2$ and n water molecules in gas state to the solid hydrate with n crystal waters, i.e., $\Delta H = \Delta_r H_{CaCl_2 \cdot n\,H_2O}$. For both liquid and solid states, *GSD* was then determined from Eq. (3).

The bulk density of different compositions ρ_{bulk} was estimated by filling a 10 ml measuring cylinders with different compositions and recording the changes in mass. Void fraction, which is sometimes called (powder) porosity, was then determined as

$$\varphi_V = 1 - \frac{\rho_{bulk}}{\rho_{capsule}} \tag{4}$$

where the average capsule solid density $\rho_{capsule}$ was determined for each composition as

$$\rho_{capsule} = \frac{1}{\frac{x}{\rho_{SiO2}} + \frac{1-x}{\rho_{aq}}} \tag{5}$$

where x is the mass fraction of SiO_2 on wet basis, determined as $x = \frac{m_{SiO2}}{m_{SiO2} + m_{CaCl_2} + m_{H_2O} + m_{EtOH}}$ with $m_{EtOH} = \rho_{EtOH} V_{EtOH} \approx 789\,\frac{\mathrm{kg}}{\mathrm{m}^3}\cdot V_{EtOH}$. The solid density of fumed silica particles is $\rho_{SiO2} = 2200\ \mathrm{kg/m^3}$ [22] and ρ_{aq} is the density of the aqueous solution used to make the composition. Since the amount of ethanol added to the compositions was small, addition of ethanol was only assumed to affect the mass fraction of $CaCl_2$ in the solution and thus, ρ_{aq} was calculated with the correlation presented in [24].

Average volume fraction of SiO_2 in the capsules was determined as

$$\varphi_{SiO_2,caps} = \frac{\frac{x}{\rho_{SiO_2}}}{\frac{x}{\rho_{SiO_2}} + \frac{1-x}{\rho_{aq}}} \tag{6}$$

Liquid volume fraction, which is the fraction of liquid solution volume in the bulk porous material, was then determined as

$$\varphi_{liq} = (1 - \varphi_V)\left(1 - \varphi_{SiO_2,caps}\right) \tag{7}$$

Volumetric energy storage density (*VSD*) was determined by assuming that the encapsulation is performed with a liquid solution that has the same hydration level as the salt will achieve when it's in equilibrium with the surrounding water vapor at the hydration conditions, i.e., it was assumed that the composite material expands to its original volume after hydration. Note that this essentially means that the composition is optimized for the expected hydration conditions already during preparation and lower *VSD* values will likely be achieved if such optimization is not done. *VSD* was determined as

$$VSD = \varphi_{liq} GSD_{wet} \rho_{aq,eq} = \varphi_{liq} \frac{\Delta H}{M_{CaCl_2}} \xi_{eq} \rho_{aq,eq} \tag{8}$$

where $GSD_{wet} = GSD\cdot\xi_{eq}$ is the gravimetric energy storage density on wet basis while ξ_{eq} is the $CaCl_2$ mass fraction and $\rho_{aq,eq}$ is the density of the $CaCl_2$-water mixture inside the capsules, with both ξ_{eq} and $\rho_{aq,eq}$ taken at the hydration conditions in equilibrium with the surrounding water vapor.

3. Results and discussion

3.1. *Morphological properties*

All preparation methods used produced a white powder-like substance which could easily be poured from one container to another. Small liquid stains could be observed on glass surfaces after pouring, suggesting that some capsules had broken. However, the amount of leaked solution was extremely small. Upon holding the samples in the glass containers for over a year, no further leakage was observed by visual inspection.

Optical microscope images (Fig. 2 and Fig. S2) show that most capsules are white and somewhat translucent. The non-spherical shape of most capsules is likely due to the silica particles jamming together at the air-liquid interface preventing the droplet from relaxation into spherical geometry [23,29]. However, there were some near perfectly spherical capsules that were often almost completely transparent. While at least some transparent capsules with diameters usually much less than 50 μm were visible on all compositions, the transparent spherical capsules were by far most prevalent on inv-2.0 (Fig. 2a) with diameters reaching 200

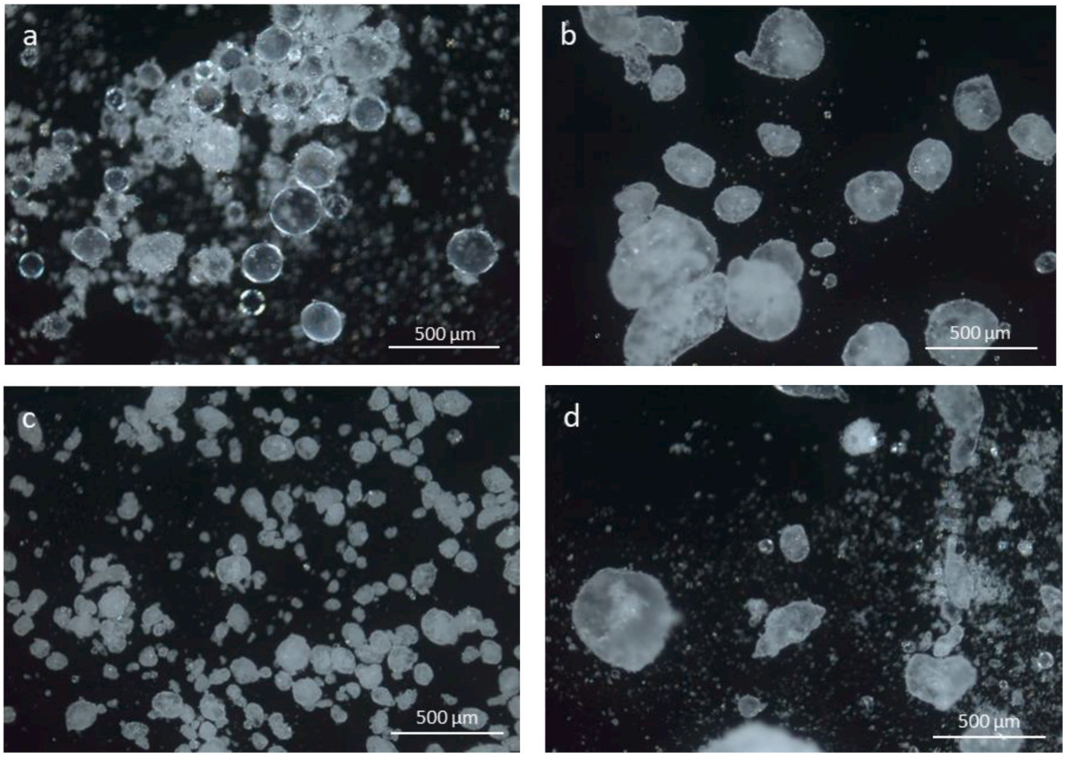

Fig. 2. Optical microscope images of composition a) inv-2.0 b) inv-2.5 c) inv-4.9 d) dir-4.9.

µm. The spherical shape in combination with transparency suggests that the nanoparticle aggregates in these capsules are not strongly entangled, allowing the liquid to relax to a spherical shape. However, we expect that nanoparticles still exist on the interface as the droplets should not be stable otherwise. It has also been found elsewhere that fumed silica nanoparticles can create nearly transparent systems [22].

The higher prevalence of the spherical, near transparent capsules on inv-2.0 seen in Fig. 2a might be due to the higher mass fraction $CaCl_2$ solution used for their preparation. Higher salt mass fraction leads to higher viscosity and higher surface tension, even though the latter effect is uncertain as the effect of the surfactant (ethanol) might eliminate the difference in surface tension. Still, these differences could make larger capsules with incomplete surface coverage more durable during the preparation, leading to a higher chance of them surviving under the shear forces endured during the mixing.

To study the morphology in detail, SEM images of different compositions were taken. The lower magnification SEM images presented in Fig. 3 confirm the irregular shape of most of the capsules. These images also suggest that higher silica content leads to lower particle size while the phase inversion method (Fig. 3a and b) results in a narrower distribution in particle size compared to the direct mixing method (Fig. 3c). Similar differences between inv-4.9 and dir-4.9 are also visible in the optical images (Fig. 2c and d). However, the optical images suggest that inv-2.0 has a smaller particle size than inv-2.5 (Fig. 2a and b), breaking the trend of higher silica content leading to smaller particle size. This is possibly due to incomplete surface coverage on capsules of inv-2.0 which would allow more surface area to be encapsulated with the same amount of silica.

The higher magnification SEM images shown in Fig. 4 show that the coating consists of SiO_2 nanoparticles that are at least partly agglomerated. Some of the SiO_2 agglomerates appear around 20 µm in size (Fig. 4a and d) which is consistent with the agglomerate sizes found in pure fumed silica powders [15,22]. However, the agglomerates may also be small capsules attached to larger ones.

Some pores of over 1 µm are visible on the surface of the larger capsule's shells (Fig. 4d) indicating that mass transfer through the shell is not completely limited to Knudsen diffusion, unless the materials are used at low total pressures. The structures of the shells seem similar for

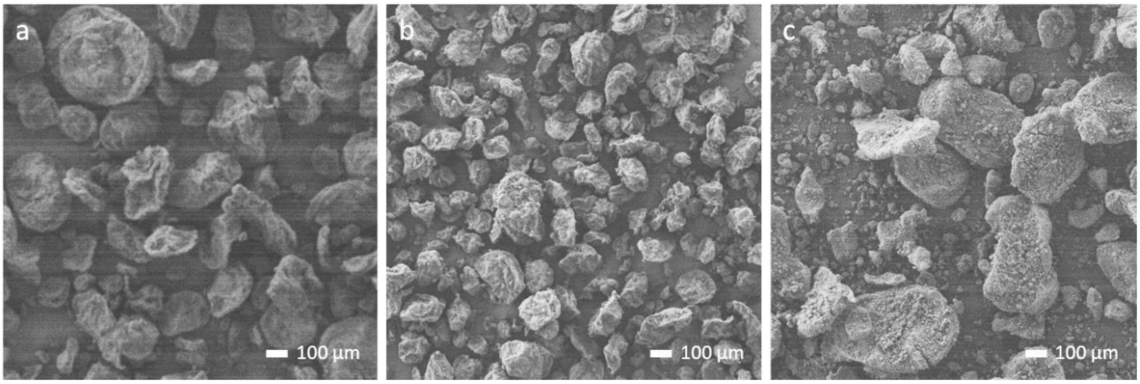

Fig. 3. Low magnification SEM images of sample a) inv-2.5 b) inv-4.9 c) dir-4.9 to illustrate particle size distribution.

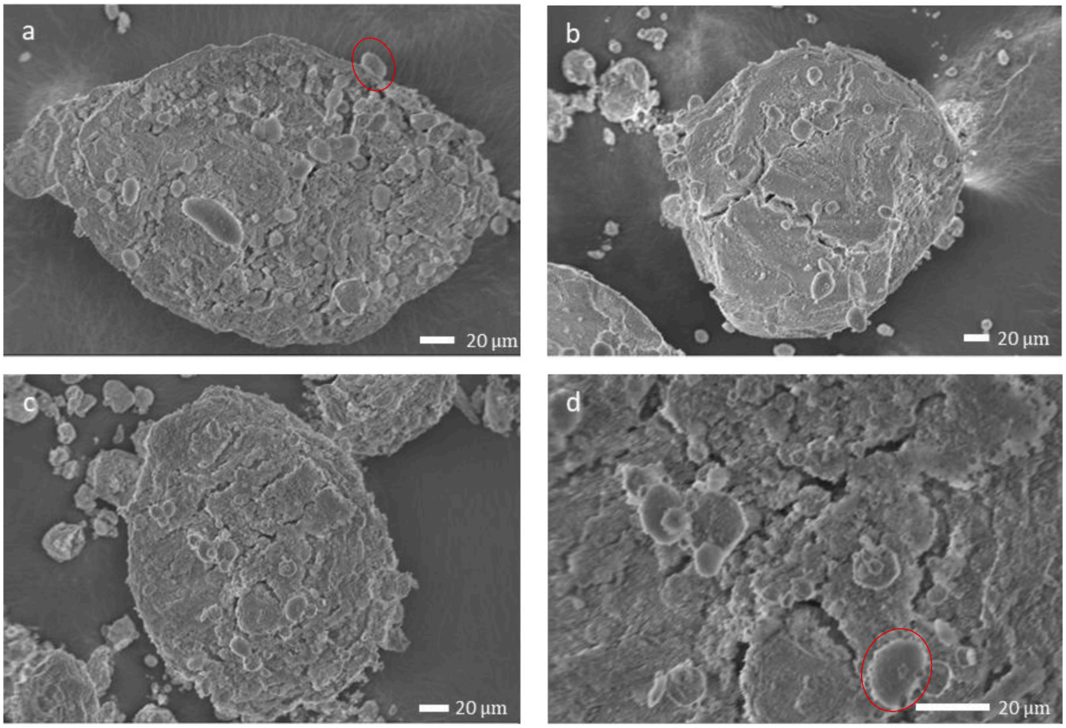

Fig. 4. SEM images of samples a) inv-7.2 b) inv-2.0 c) dir-4.9 d) section of dir-4.9 magnified further. Red circles highlight possible larger SiO_2 agglomerates. (For interpretation of the references to color in this figure legend, the reader is referred to the Web version of this article).

different compositions except for inv-2.0 for which the surfaces appear smoother with some larger cracks (Fig. 4b). This is likely due to the thinner and more incomplete surface coverage of nanoparticles on these capsules which allows the salt surface to be visible.

The particle size distributions from laser diffraction measurements shown in Fig. 5 further confirm the narrower spread in particle size with the phase inversion method. Apart from inv-2.0, only one strong peak is visible for compositions made with the phase inversion method while the compositions made with the direct mixing method show two strong peaks resulting in a wider spread. For inv-2.0 there appears to be two overlapping peaks. The cause for this is unknown but it is perhaps related to the incomplete encapsulation of some capsules.

The difference in particle size distribution spread is especially high for samples with 4.9 wt% silica with dir-4.9 showing a much higher share of large capsules with size over 300 μm than inv-4.9. It is known that for liquid marbles, which are millimeter sized liquid droplets encapsulated with nonwetting particles, durability under compression pressure increases linearly as radius decreases [30]. Thus, the phase inversion method, which produces less of the larger particles, might be more desirable for systems where the capsules are under relatively large pressures, for example under the weight of the capsules above them or while enduring collisions with container walls and other capsules in a fluidized bed type reactor.

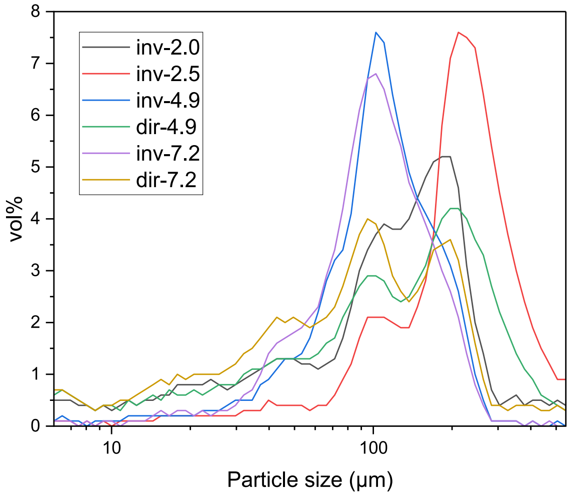

Fig. 5. Particle size distributions of different compositions measured with laser diffraction.

The volume median diameters ($D_{V,0.5}$) and 90th percentiles ($D_{V,0.9}$), i.e. particle size below which 90% of the volume distribution is located, are shown in Table 3. These were determined via laser diffraction measurements. Overall, $D_{V,0.5}$ of dried capsules of different compositions ranged from around 90 to 210 μm. $D_{V,0.5}$ generally decreases with increasing silica content, especially when going from inv-2.5 to inv-4.9. However, as an exception to this rule, inv-2.0 displays a much smaller $D_{V,0.5}$ than inv-2.5. This further suggests that the capsule shells in inv-2.0 are thinner and less densely covered with silica than in inv-2.5.

After dispersing the sample in kerosene, $D_{V,0.5}$ decreased with time when repeated measurements were taken, suggesting that larger particles may have been slowly sedimenting beneath the laser light despite the mixing with magnetic stirrer. Thus, it is possible that some larger capsules were not detected as accurately as the smaller ones.

Table 3
Volume median diameter ($D_{V,0.5}$) and 90th percentiles ($D_{V,0.9}$) of dried compositions based on laser diffraction measurements and BET surface area of dried compositions and fumed silica (Aerosil R812S).

Composition	$D_{V,0.5}$ (μm)	$D_{V,0.9}$ (μm)	BET surface area (m^2/g)
inv-2.0	119	226	8.3
inv-2.5	212	353	7.4
inv-4.9	106	188	12.5
dir-4.9	121	287	12.2
inv-7.2	101	180	17.6
dir-7.2	86	212	16.1
fumed silica	–	–	224

The results of BET surface area analysis are included in Table 3. The measured BET surface area of Aerosil R812S (223.8 m^2/g) corresponds well with the manufacturer's reported range of 195–245 m^2/g [22]. For the composites, an increasing silica content seems to lead to an increase in surface area. This is likely due to two factors. First, as shown earlier, an increase in silica content leads to smaller capsule size and therefore an increase in overall surface area of a sample. Thus, the BET results further confirm this correlation between particle size and silica content. Second, fumed silica has a very high specific surface area so any increase in the amount of silica will be visible in the results. However, composition inv-2.0 deviates from the general trend as its BET surface area is higher than that of inv-2.5. This further confirms the smaller particle size of inv-2.0 compared to inv-2.5 found in laser diffraction measurements.

Fig. 6 shows EDX mapping indicating the presence of calcium and silicon on composition dir-7.2. Calcium can be seen spread rather evenly on the entire surface. The varying intensity of silicon indicates that the thickness of the silica layer varies on the surface, even on dir-7.2 which has a relatively high silica content. When comparing Fig. 6 and Fig. S3 it can be seen that the intensity of chloride matches well with that of calcium which is expected as they are chemically bonded and thus cannot exist separately. Similarly, silicon and oxygen intensities match well due to chemical bonding of the elements. A layered image showing a combination of the different elements is shown in Fig. S4 and EDX elemental diagram is shown in Fig. S5. X-ray patterns of the dried fumed silica encapsulated $CaCl_2$ (composition dir-4.9) and pure fumed silica are also shown in Fig. S6.

3.2. Sorption properties

The sorption properties depicting the material's ability to absorb water and release heat are collected into Table 4 for different compositions and pure $CaCl_2$. Measurements were made at a hydration temperature of 30 °C with water vapor pressure set to ~1.3 kPa. At least one sample from both prepared batches of each composition was measured to ensure repeatability. Equilibrium values of the mass fraction of $CaCl_2$ in the solution $\xi_{eq} \approx 0.443$ and hydration level $n_{eq} \approx 7.76$, corresponding to the measured water intake $w \approx 1.26$ of pure $CaCl_2$, were used in calculating ΔH and GSD with Eqs. (2) and (3). Note, that the measured heat release per mass of dry sample q is technically an estimate of GSD as well but due to known underestimation of hydration reaction heats explained earlier in Chapter 2.5, GSD estimate is given based on measured water intake w and Eqs. (2) and (3) while q is used to calculate ER.

As can be seen in Table 4, values of both encapsulation ratio ER and sorption ratio SR determined based on STA measurements correlate with the amount of SiO_2 used for each composition. Thus, the values suggest that the encapsulation was complete in all compositions and that the presence of SiO_2 nanoparticles does not significantly affect the sorption properties of $CaCl_2$. Based on the difference between values of q and GSD of pure $CaCl_2$, STA seems to underestimate reaction heats by about 4%.

The equilibrium hydration level of inv-2.0 calculated with Eq. (1) based on STA measurements at different water vapor pressures at 30 °C is shown in Fig. 7. The formation of a solid dihydrate took place at low vapor pressure below 0.3 kPa. Once vapor pressure of 0.92 kPa, which is the vapor pressure of a saturated solution of $CaCl_2$ at 30 °C, was reached, the salt inside the capsules behaved as can be expected for an aqueous $CaCl_2$ solution, i.e., hydration level followed the known relationship between water vapor pressure and $CaCl_2$ mass fraction.

However, conversion to solid tetrahydrate was not found at any vapor pressure. Instead, as vapor pressure was increased above a threshold level of ~0.68 kPa, $CaCl_2$ inside the capsules reached a hydration level of 5.16 which could then be continuously increased and decreased back by altering the vapor pressure slightly. Thus, it seems very likely that the $CaCl_2$ inside the capsules was in liquid state.

The $CaCl_2$ mass fraction in this solution was clearly over the

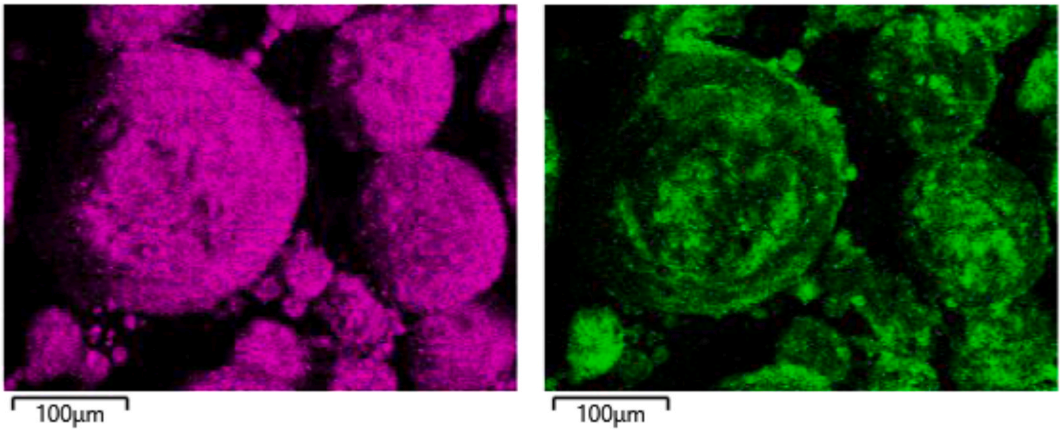

Fig. 6. EDX mapping of dir-7.2. The two images are of the same area in the sample. Purple color on the left-hand image shows presence of calcium while the green color on the right-hand image indicates presence of silicon. (For interpretation of the references to color in this figure legend, the reader is referred to the Web version of this article).

Table 4
Measured heat released in STA per mass of dry sample (q), encapsulation ratio (ER), equilibrium water intake (w), sorption ratio (SR) and the estimated GSD based on w and thermodynamic properties of $CaCl_2$. All values are based on measurements at a hydration temperature of 30 °C with water vapor pressure set to 1.3 kPa.

Composition	q, measured on STA (J/$g_{dry\ sample}$)	ER	w (g/g)	SR	GSD, based on w (J/$g_{dry\ sample}$)
pure $CaCl_2$	3494 ±77	1.000	1.26 ± 0.007	1.000	3638
inv-2.0	3408 ±65	0.975	1.23 ± 0.008	0.981	3567
inv-2.5	3386 ± 49	0.969	1.23 ± 0.007	0.977	3554
inv-4.9	3364 ± 18	0.963	1.20 ± 0.006	0.952	3462
dir-4.9	3278 ± 18	0.938	1.20 ± 0.001	0.956	3478
inv-7.2	3202 ± 3	0.916	1.17 ± 0.004	0.931	3387
dir-7.2	3206 ± 1	0.917	1.17 ± 0.003	0.935	3402

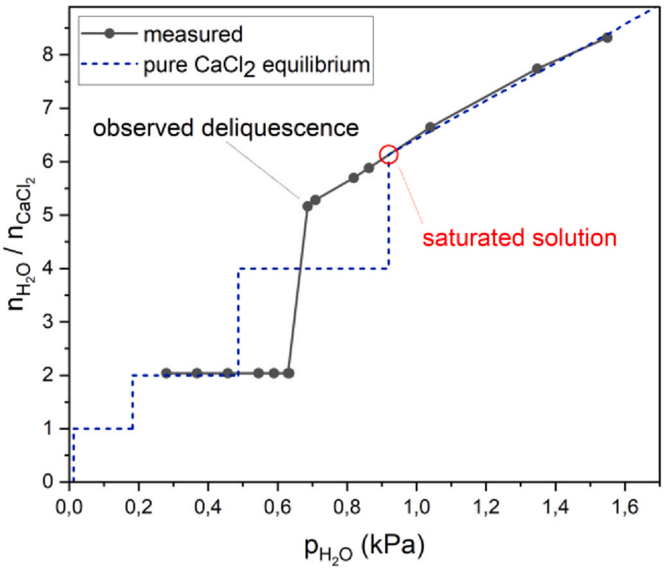

Fig. 7. Measured equilibrium hydration level of inv-2.0 at 30 °C at different water vapor pressures with pure $CaCl_2$ equilibrium shown for comparison. Equilibrium properties of pure $CaCl_2$ equilibrium are based on [24,31]. Although a hydrate of form $CaCl_2 \cdot (1/3)\ H_2O$ is also known to exist [26], it was left out of for simplicity.

solubility limit of ~50% at 30 °C [24]. Thus, it seems that the formed solution inside the capsules is supersaturated and forms at a relative humidity value that is much smaller than the DRH that would be expected based on the thermodynamic equilibrium. In recent years, it has been found that small samples of $CaCl_2$ can deliquesce into supersaturated solutions at far lower RH values than the vapor pressure of a saturated $CaCl_2$ solution would suggest [32,33]. As relative humidity is increased, due to deliquescence being a much faster process than the formation of a higher solid hydrate (tetrahydrate or hexahydrate), the dihydrate can deliquesce before the sample has time to hydrate to a higher solid hydrate in any measurable amount [32]. This can occur since the dihydrate has a lower DRH than the higher hydrates and due to nucleation barrier preventing crystallization, the formed metastable liquids may not crystallize into the thermodynamically stable hydrate for very long periods of time. The phenomenon appears to be more common the smaller the salt particle is [32]. Since the hydrophobic silica capsules create rather small particles of $CaCl_2$ (Table 3), it is likely that this phenomenon is occurring during their hydration.

To support this hypothesis, we evaluated the relative humidity at which 2–3 mg samples of inv-2.0 start to transition from dihydrate state to a higher hydration level at different temperatures ranging from 25 °C to 40 °C and measured the equilibrium hydration level just above the RH threshold level. Starting with a sample in STA dried at 150 °C and cooled to the desired temperature with only pure N_2 flow present, RH was increased at isothermal conditions to around 8% at which point the salt transitioned into the dihydrate state. Once the sample mass had stabilized to the dihydrate state, RH was increased stepwise by 1% if no notable change in mass was detected in 3 min. In these measurements, once mass gain started the samples appeared to always deliquesce and no evidence of transition onto a tetrahydrate or hexahydrate was observed at any of the temperatures. At 25 °C, deliquescence occurred at ~16% RH and at other temperatures measured (30 °C, 35 °C, and 40 °C), the measured DRH was between 15% and 17%. The results match well with the dihydrate DRH value of 18.5% measured by Guo et al. [33] at 25 °C and the value of 16% predicted by Kelly and Wexler [34] at the same temperature. Considering that Guo et al. [33] reported an absolute uncertainty of ± 1% and we estimate the absolute uncertainty to be ± 2% for RH in our measurements, both of these fall within our range of accuracy. Thus, it seems very likely that instead of going through the thermodynamic equilibrium states, during the sorption process the $CaCl_2$ particles inside the SiO_2 shells first hydrate into the dihydrate and then deliquesce into a supersaturated solution.

It is possible that the hydration to tetrahydrate was just too slow to be observed before RH was increased. However, such slow process would likely have little practical significance for sorption TCES, as heating power extractable from the reaction would be extremely low.

3.3. *Thermal conductivity*

The average thermal conductivities and corresponding standard deviations (SD) of different compositions are shown in Table 5. The standard deviation for samples within each batch was low; typically around for 0.001 W/(mK), maximum value 0.004 W/(mK) was found for wet inv-2.0 sample. Generally, the thermal conductivities are quite low as expected for a powder-type material. In wet state, i.e., when the salt inside the capsules is in an aqueous solution state, the thermal conductivities are higher. This is probably due to the higher proportional share of fumed silica in the dried state as we measured Aerosil R812S thermal conductivity in powder form to be very low (0.040 W/(mK)). Low thermal conductivity of fumed silica also explains the decreasing trend of thermal conductivity with higher silica content. However, the thermal conductivity of inv-2.0 in wet state is comparatively low. This is probably due to the higher concentration of the salt solution which decreases the thermal conductivity of the aqueous solution [24].

3.4. *Sorption kinetics*

The isothermal dehydration and hydration curves from STA measurements are shown in Fig. 8 for different compositions. The dehydration of samples when heated at a rate of 10 K/min is shown in Fig. S7.

The isothermal dehydration at 80 °C from the dihydrate state (Fig. 8a) seems to occur in two steps with on average around 1.3–1.4 water molecules per each salt molecule leaving rather quickly in less than 15 min. The complete dehydration takes up to 100 min due to the decrease in dehydration kinetics that occurs after the first 1.3–1.4 water molecules have left. The cause of the sudden decrease in dehydration kinetics around this mark is yet unknown.

Apart from inv-2.0, the dehydration kinetics improve with increasing BET surface area. In addition, apart from inv-2.0, the dehydration kinetics improve with decreasing $D_{V,0.5}$ except the order of dir-7.2 and inv-7.2 is reversed. This is likely due to the much higher share of relatively large capsules in dir-7.2 compared to inv-7.2 that can be seen in Fig. 5 and is also apparent in its much higher $D_{V,0.9}$ value. In larger capsules, there is a longer distance for water molecules to travel before they reach the crystal surface. In addition, larger capsules also have a smaller ratio of surface area to particle volume. Thus, the findings agree well with expectations from theory.

The slower kinetics of inv-2.0 might be caused by tighter packing of the particles during the dehydration. All the samples are expected to become more porous as they lose water. However, the samples were placed in the STA chamber in the condition they were after preparation and inv-2.0 is made with 56 wt% $CaCl_2$ solution while the other samples are made with a 43 wt% solution. Thus, inv-2.0 is likely less porous

Table 5
Thermal conductivities in units W/(mK) of different compositions at 23 °C in both wet and dry state.

	inv-2.0	inv-2.5	inv-4.9	dir-4.9	inv-7.2	dir-7.2
WET						
Average	0.127	0.161	0.139	0.127	0.122	0.107
SD	0.004	0.002	0.003	0.001	0.002	0.001
DRY						
Average	0.078	0.068	0.063	0.064	0.059	0.059
SD	0.002	0.001	0.001	0.001	0.001	0.001

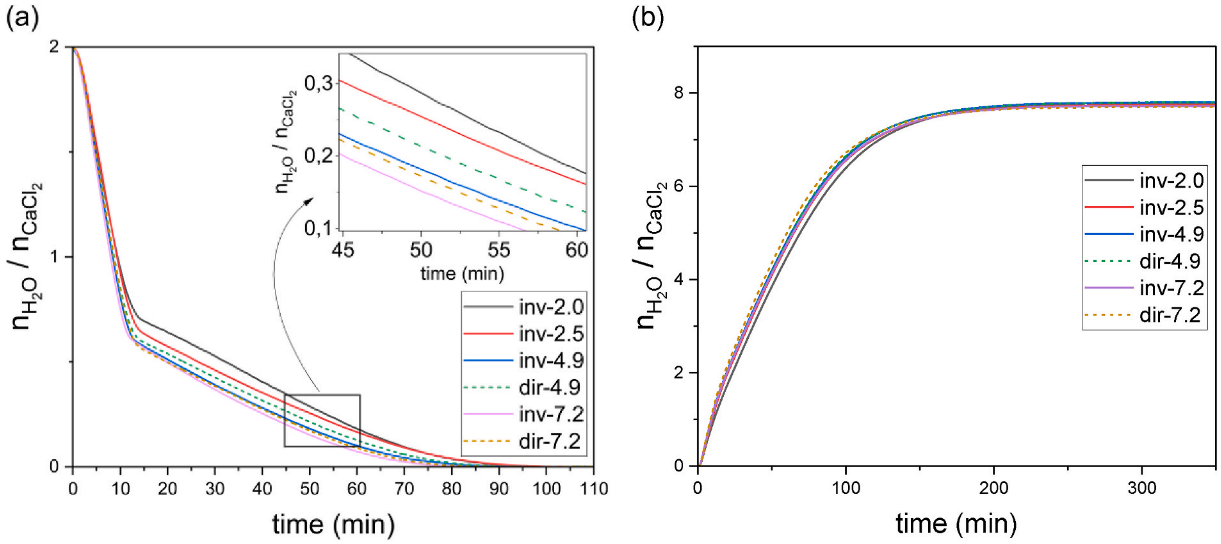

Fig. 8. (a) Isothermal dehydration of samples at 80 °C (b) Hydration curves for isothermal hydration of samples at hydration temperature T_h = 30 °C with p_h = 1.3 kPa.

during dehydration, reducing its reaction kinetics compared to the other samples.

When heating the sample at a rate of 10 K/min, the differences in dehydration kinetics were overall very small, especially for the early part of the dehydration down to around hydration level of three. To get more detailed curves, only the removal of the last three water molecules is shown in Fig. S7. It is possible that early dehydration is mainly limited by water vapor transfer from the top of the sample to STA chamber surroundings, which hides the differences between compositions. However, for the removal of the last two water molecules, inv-2.0 and dir-4.9 show slightly slower dehydration kinetics as does inv-2.5 albeit to a lesser extent. The order in kinetics of dir-4.9 and inv-2.5 is reversed from the isothermal dehydration measurements. This might be explained by larger thermal gradients forming inside the samples. With the high heating rate of 10 K/min, the samples completely dehydrate from a state with hydration level of 7.76 to anhydrous state in less than 15 min. During the dehydration, the temperature in the middle of the sample is likely smaller than on the edges due to limited heat transfer from the sample edges. The temperature gradient is amplified due to the high evaporation rate cooling down the sample. As dir-4.9 has a lower thermal conductivity than inv-2.5 (Table 5) and a lower bulk density (Table 6), i.e., the sample with same mass of $CaCl_2$ had a larger volume, larger temperature gradients are expected to form inside dir-4.9 than inv-2.5. This might have slowed down the dehydration of dir-4.9 enough to reverse the order.

Note that if the sorption material is dried by hot air flowing through it, as is often the case for sorption systems, differences in powder thermal conductivity will not affect the dehydration kinetics as they have here. Thus, results from the isothermal dehydration experiments are more relevant for most practical applications.

The isothermal hydration kinetics are depicted in Fig. 8b. The hydration kinetics overall show quite small differences between different samples. However, even considering for possible inaccuracy in measurements, inv-2.0 does show somewhat slower kinetics than the others. As with dehydration kinetics, this might be due to the tighter packing of this composition.

Despite the small differences observed here, the compositions might show significantly larger differences in hydration kinetics in practical scale storage systems. Since there is no gas flow through the powder sample inside the STA chamber, reaction kinetics might be mainly limited by water vapor transfer external to the capsules rather than internal transfer or reaction kinetics. In practical scale storage systems humid air would be flown through the powder or the powder would be placed in near-vacuum conditions. In both cases it is expected that particle size would affect reaction kinetics to a much higher degree, although this will have to be confirmed with further studies.

3.5. Cycling stability

All compositions were tested for cycle stability in repeated dehydration – hydration cycles which is crucial for long-term performance of the material. For each composition, at least one sample from both prepared batches of each composition was tested to ensure repeatability of the preparation method. Fig. 9a shows the thermogravimetric analysis and temperature curves for cycling experiments with inv-2.5 and Fig. 9b shows the relative water intake α_i for each cycle i for different compositions. Similar graph for compositions with 7.2 wt% SiO_2 is included in Supplementary information (Fig. S8). All tested samples showed excellent stability under 10 repeated cycles. Furthermore, inv-2.0 showed no signs of degradation under 30 cycles as shown in Fig. S9. As inv-2.0 has the lowest amount of silica in the composition, it was expected to be the most susceptible to degradation due to agglomeration. Thus, it is very

Table 6
Densities and volume fractions of different compositions. The bulk density ρ_{bulk} is based on measurements with volumetric flask. Eqs. (4)–(7) are used for determining φ_V, $\rho_{capsule}$, $\varphi_{SiO_2,caps}$ and φ_{liq}. Density of aqueous solution ρ_{aq} is based on the correlation presented in [24].

Composition	x	$\varphi_{SiO_2,caps}$	ρ_{bulk} (g/ml)	ρ_{aq} (g/ml)	$\rho_{capsule}$ (g/ml)	φ_V	φ_{liq}
inv-2.0	0.0111	0.008	1.05	1.57	1.58	0.34	0.66
inv-2.5	0.0106	0.007	1.04	1.41	1.42	0.27	0.72
inv-4.9	0.0210	0.013	0.84	1.41	1.42	0.41	0.58
dir-4.9	0.0212	0.014	0.86	1.42	1.43	0.40	0.59
inv-7.2	0.0315	0.020	0.74	1.41	1.43	0.48	0.51
dir-7.2	0.0318	0.021	0.69	1.42	1.44	0.52	0.47

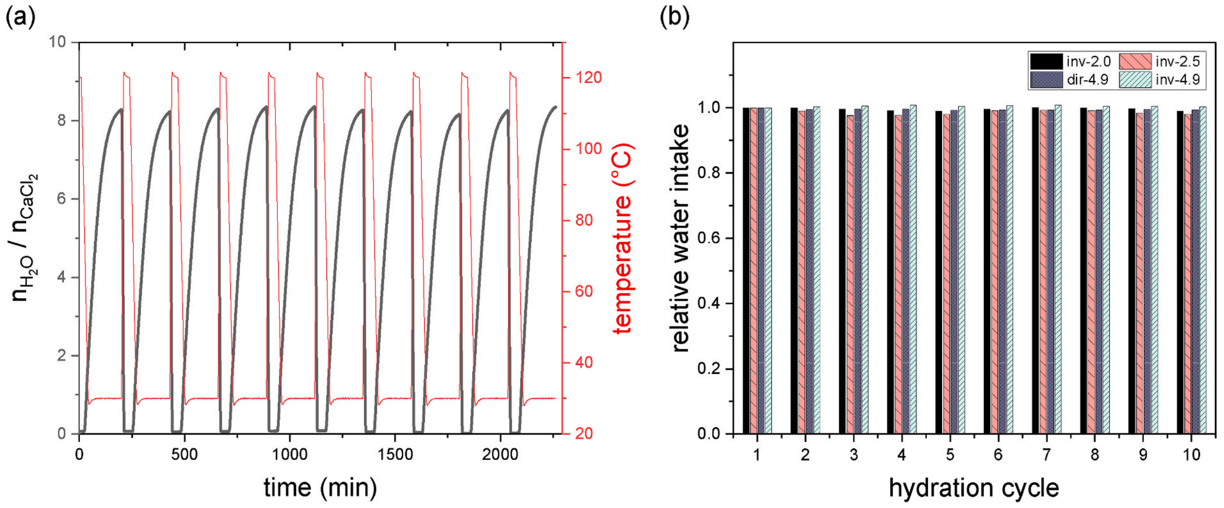

Fig. 9. (a) Ten dehydration/hydration cycles for inv-2.5. Water vapor pressure was set to 1.5 kPa. (b) Relative water intake for each hydration cycle for different samples.

likely that all the other compositions would perform equally well.

The test conditions were such that $CaCl_2$ went through complete dissolution during the hydration step. Thus, any significant breakage of the capsules should have led to liquid solution escaping the capsules and contacting other leaked liquid, leading to significant agglomeration upon recrystallization during the subsequent heating step. If this had occurred, a notable declining trend in the hydration level at the end of each sorption step should have been visible, as hydration kinetics would have been hindered. However, no such trend was found within measurement accuracy; even for the measurement with the most decrease in relative water intake (sample of inv-2.5, shown in Fig. 9b), the last hydration showed over 98% water intake compared to the first cycle, i.e. $\alpha_{10} > 0.98$ while another sample of the same composition (shown in Fig. 9a) resulted in $\alpha_{10} \approx 1.01$.

The results in Fig. 9, Fig. S8 and Fig. S9 show that the capsules are very stable and very little if any solution is leaking out of them at any stage. Thus, agglomeration seems to be completely prevented. The capsules were durable even under conditions where they expanded beyond their original volume, as inv-2.0 was prepared with a 56 wt% $CaCl_2$ solution but hydrated to a less than 43.5 wt% solution during the hydration steps, corresponding to 41% increase from original capsule volume. Previously, Liu et al. [30] have shown that liquid marbles made from Aerosil R812 hydrophobic fumed silica can withstand almost 45% increase in surface area upon deformation under compression before rupturing due to eventual poor surface coverage of particles on its surface. It seems likely that due to the core of dry water-style capsules being made of a liquid, and the nanoparticle aggregates not strongly attached to one another, the aggregates can rearrange themselves on the surface. This ensures that enough of the surface remains covered to prevent liquid leakage and agglomeration to other capsules even if the volume and thus also surface area of the capsules expands to some extent. If we assume encapsulated salt solutions have similar durability as encapsulated water droplets, the encapsulated salts might last expanding by up to 75% from original volume, although the limits were not tested in this study.

3.6. Sample density

Measured bulk densities of different compositions (ρ_{bulk}) are shown in Table 6. The values listed are measured without any tapping or shaking apart from very lightly shaking the cylinder to even the top layer of the powder for measurements. It was found that density could be increased by slightly tapping or shaking the measuring cylinder. For example, for the inv-2.5 the density could easily be increased up to 1.12 g/ml, i.e., by almost 8% with this method. This is likely due to the capsules reorienting themselves to a denser packing under the shaking. It is also possible that the capsules, containing a deformable liquid solution and inside a shell consisting of separate nanoparticles, might be reshaped slightly upon tapping.

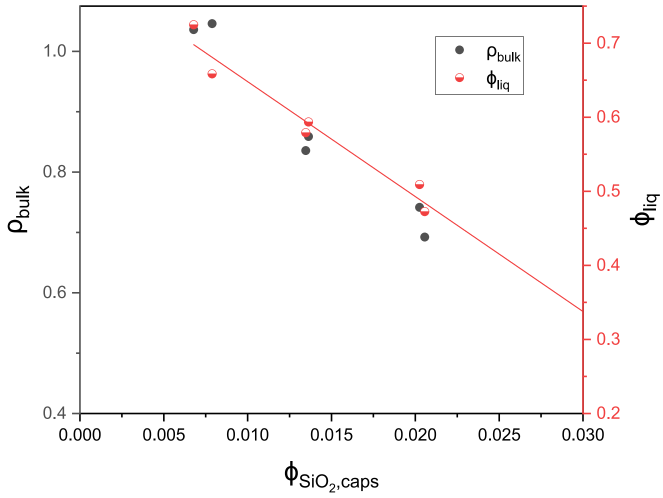

Fig. 10. Bulk density of composition and liquid volume fraction in different compositions as a function of average volume fraction of silica nanoparticles in the capsules. Linear fit is made for φ_{liq}.

Results for densities and volume fractions can be found in Table 6. ρ_{bulk} and φ_{liq} are plotted as a function of $\varphi_{SiO_2,caps}$ in Fig. 10, which shows that both ρ_{bulk} and φ_{liq} correlate negatively with increasing volumetric fraction of SiO_2 in the capsules. However, no significant difference between the two preparation methods can be seen. Strong negative correlation between volumetric fraction of SiO_2 and bulk density was also observed by Binks and Murakami [13], who found that the bulk density of dry water dropped by a factor of 2.5 when silica content was increased from 2 wt% to 9 wt%. The strong decrease in bulk density with increasing silica content is likely caused by the highly porous structure of the branched fumed silica aggregates. This porous structure should lead to very low bulk density for the shell of the capsules as well as for any fumed silica agglomerates that remain between the capsules. This is supported by the extremely low bulk density of fumed silica. For Aerosil R812S the bulk density is only 60 g/l [22] i.e., over 97 vol% of Aerosil

R812S powder is air and similar void fraction may be present in the capsule shells. As can be seen from Eq. (8), *VSD* is directly proportional to φ_{liq} and therefore the best composition inv-2.5 should have over 53% higher *VSD* than inv-7.2 which has the lowest φ_{liq}.

3.7. Energy storage density

Values of gravimetric energy storage density (*GSD*) and volumetric energy storage density (*VSD*) are some of the most important criteria for feasibility of long-term TCES systems as they highly affect the cost of the system and storage space required. For calculation of *GSD* from Eq. (3) and *VSD* from Eq. (8), tetrahydrate and hexahydrate are neglected as they are not expected to form based on the STA measurements. Thus, the only solid hydrates that are expected to form during the hydration are the monohydrate and the dihydrate. Once sufficient RH for solid dihydrate formation is achieved, further increase in water vapor pressure leads to formation of a supersaturated solution once the dihydrate DRH is reached. Based on Fig. 7 and values of *w* recorded at the DRH limit at different temperatures, the correlation presented in [24] should provide accurate predictions even for the supersaturated solutions with absolute uncertainties of less than 2% in RH. Thus, the predictions of *GSD* and *VSD* should have good accuracy.

As data on the dihydrate melt density could not be found, a rough density estimate $0.8{\cdot}\rho_{CaCl_2\cdot 2\ H_2O} = 1.48\ \text{g/cm}^3$, where $\rho_{CaCl_2\cdot 2\ H_2O}$ is the density of solid dihydrate, was used for determination of *VSD* of the dihydrate. This estimate may be optimistic as the encapsulation would have to be done at very high temperature above the melting point of the dihydrate $T_m = 176\ ^\circ\text{C}$, which has not been tested and as such, a solution with lower mass fraction of $CaCl_2$ may be needed so that the composition can be prepared at a lower temperature. For the monohydrate, a diluted solution with a weight fraction of the dihydrate and density of 1.48 g/cm^3 was assumed for the encapsulation.

As can be seen in Table 6, $\varphi_{liq,inv-2.0} = 0.66 < \varphi_{liq,inv-2.5} = 0.72$, even though the two composites have similar $\varphi_{SiO_2,caps}$. Thus, the use of higher mass fraction of $CaCl_2$ in preparation may affect the achievable liquid volume fraction. To avoid overly optimistic estimates in some conditions, $\varphi_{liq} = 0.66$ was used to calculate *VSD*. For *GSD*, $SR = 0.975$, i.e., the *SR* value of inv-2.5 was used. Both *GSD* and *VSD* are plotted as a function of dew point in Fig. 11. The horizontal lines in both graphs are due to the dihydrate and monohydrate reaction enthalpies and densities which vary very little with hydration temperatures. Therefore, lines for different hydration temperatures overlap. The horizontal lines extend beyond the plotted dew point range as the lower hydrates can form even with dew point below $T_{dew} = -7\ ^\circ\text{C}$.

It can be seen from Fig. 11 that increasing the water evaporation temperature (dew point T_d) with constant hydration temperature (T_h), i.e., decreasing the temperature lift ($T_h - T_d$) will increase *GSD* exponentially once deliquescence threshold is achieved but *VSD* does not increase much and eventually peaks and starts to decrease. This is due to the increase in volume that occurs with each absorbed water molecule and the decrease in density as the mass fraction of salt in the solution gets lower. Additionally, the heat released per absorbed water molecule gets lower and eventually approaches water condensation heat as the salt mass fraction approaches zero, i.e., when the dew point gets close to the hydration temperature.

Based on Fig. 11a, *VSD* values of 0.82 GJ/m^3 are achievable even with high temperature lifts exceeding 60 °C as $CaCl_2$ hydrates to the dihydrate stage with very low water vapor pressures. With temperature lifts of around 30 °C it should still be possible to achieve high *VSD* values of around 1.4 GJ/m^3. Such high *VSD* values easily exceeding 1 GJ/m^3 have not been reported elsewhere in sorption energy storage literature to our knowledge. To put the results into context, Donkers et al. [4] suggest that 7–12 GJ of thermal energy storage capacity is needed to overcome seasonal fluctuations on a typical Western European 120 m^2 residential building, assuming the passive house standard of 15 kW h/m^3 or 28 kW h/m^3 for built or renovated buildings respectively, is applied. Based on an evaporation temperature of 10 °C, which according to Donkers et al. [4] is a reasonable estimate for temperature at which water can be evaporated if a 7 m deep borehole in the Netherlands is used as the heat source, and a hydration temperature of 30 °C, *VSD* of just over 1.5 GJ/m^3 could be achieved with inv-2.5. This suggests that in some cases less than 5 m^3 of material storage space would be needed for storing solar heat for the whole winter in new, well insulated buildings.

Based on Fig. 11b, *GSD* values of around 1100 kJ/kg are achieved if only dihydrate forms but with temperature lifts of around 30 °C, *GSD* is around 2400 kJ/kg. The latter value is higher than what is usually achievable even with pure $CaCl_2$ in similar conditions as the highest hydrate that can achieve a temperature lift of 30 °C is the tetrahydrate, for which *GSD* ≈ 2200 kJ/kg. The increase in *GSD* for the composite is due to the early deliquescence and resulting higher hydration level compared to the stable tetrahydrate (Fig. 7). The difference between the composite material and pure $CaCl_2$ gets even larger when vapor pressure is increased but is kept below the vapor pressure of a saturated $CaCl_2$ solution. For example, the maximum difference at hydration temperature of 30 °C occurs when the vapor pressure is 0.91 kPa (dew point 5.6 °C), i.e., just below the vapor pressure of saturated $CaCl_2$ solution. At

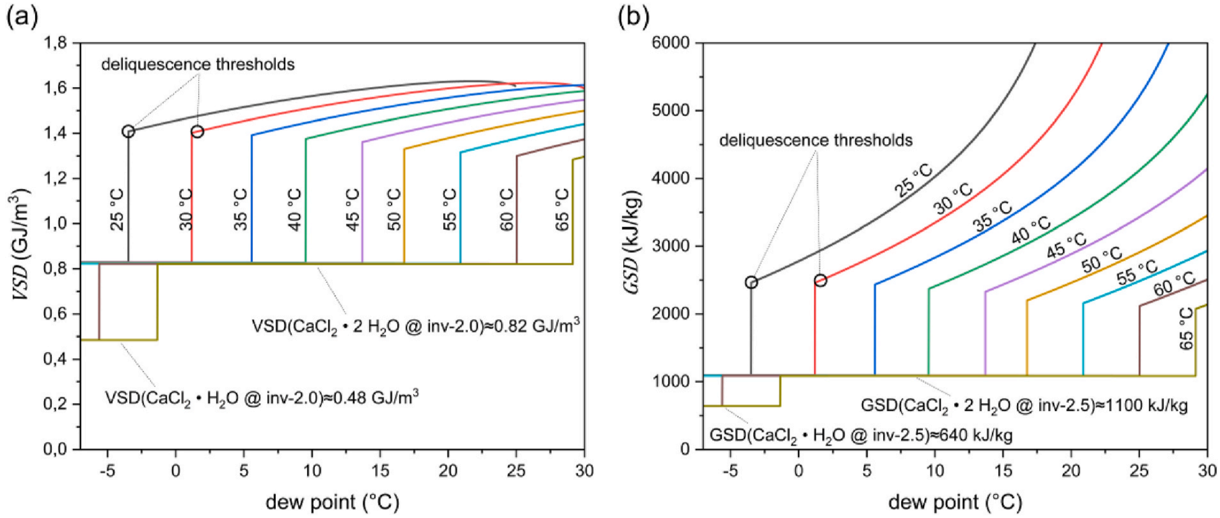

Fig. 11. (a) Volumetric energy storage density and (b) gravimetric energy storage density achievable at different output temperatures as a function of dew point. Deliquescence thresholds are present on all curves even though they are marked only on isotherms of 25 °C and 30 °C.

Table 7
Comparison of *GSD* and *VSD* of other state-of-the-art sorption materials to that of inv-2.5 ($GSD_{inv-2.5}$ and $VSD_{inv-2.5}$). Salt content is for the referenced materials, inv-2.5 has a salt content of 97.5 wt%. T_d and T_h are the dew point and hydration temperature respectively and they are the same for the referenced material and our material.

Composite	salt content (wt%)	T_d/T_h	*GSD* (kJ/kg)	$GSD_{inv-2.5}$ (kJ/kg)	*VSD* (GJ/m^3)	$VSD_{inv-2.5}$ (GJ/m^3)
$CaCl_2$@MIL-101(Cr) [35]	62	10/30	1606[a]	3345	1.03[a]	1.51
$CaCl_2$@hollow SiO_2 [6]	50	13/45	1100	2330[b]	0.9	1.36[b]
$CaCl_2$@silica gel [36]	43	10/30	1080	3345	0.76	1.51
LiCl@hollow SiO_2 [6]	45	13/60	630	1088	0.5	0.82
LiOH/LiCl@expanded graphite [37]	65.8	15/40	1075[a]	2860	0.77[a]	1.45
K_2CO_3@expanded vermiculite [38]	69	25/40	–	4116	0.9[c]	1.55
$MgCl_2$@zeolite [39]	22	22/30	1368	5879	1.11	1.61

[a] Value from 10th cycle as there was some degradation in the material.

[b] Hydration conditions are just on the DRH limit of our material. In the cited study [6], the conditions were similarly on a threshold where hydration took a step up. Thus, the higher estimate where deliquescence takes place is given.

this point, *GSD* ≈ 2850 kJ/kg which is 30% higher than the *GSD* of the stable form of $CaCl_2$ in these conditions, i.e., the tetrahydrate. For the temperature lift from 10 °C to 30 °C, *GSD* is over 3300 kJ/kg.

In Table 7, the *GSD* and *VSD* of our composition inv-2.5 is compared to the best performing salt hydrate sorption composites reported in recent reviews [5,6]. The comparison is done by determining $GSD_{inv-2.5}$ and $VSD_{inv-2.5}$ under the same hydration conditions, i.e., with the same T_d and T_h as used in the referenced studies. Only those composites studied under conditions of $T_h > 20$ were considered as lower temperatures were not considered reasonable for domestic heating applications. $GSD_{inv-2.5}$ and $VSD_{inv-2.5}$ are determined based on Eqs. (3) and (8) similarly as was done for Fig. 11 with $SR = 0.975$ and $\varphi_{sol,liq} = 0.66$. Clearly, inv-2.5 is expected to perform notably better than any other state-of-the-art composite in all studied hydration conditions. Furthermore, the low content of additive material should keep costs low.

While Fig. 11 details a conservative estimate for *VSD*, values higher by 9% are estimated if the measured solution volume fraction of inv-2.5, $\varphi_{liq,2.5\ p.i.} = 0.72$, is used. If we also assume that the density increase achieved by tapping and shaking the powder is achievable in energy storage applications, 18% increase in *VSD* can be achieved as solution volume fraction would increase to $\varphi_{liq} = 0.78$. Thus, with water evaporation temperature at 10 °C and a hydration temperature of 30 °C, values as high as *VSD* ≈ 1.8 GJ/m^3 might be achievable. However, the effects of such density increase to kinetic properties and capsule stability will need to be confirmed in another study.

4. Conclusions

In this work, we showed that $CaCl_2$ can be encapsulated with hydrophobic fumed silica nanoparticles to create capsules that prevent liquid $CaCl_2$ solution from leaking out while still allowing water vapor to permeate. As a result, the new material composite provides exceptionally promising properties for long-term thermal energy storage.

Two different methods, direct mixing method and phase inversion method, both with varying amounts of silica, were compared. The structural properties of formed capsules were investigated with various methods including optical microscopy, SEM and laser diffraction confirming the encapsulation of the salt into capsules with volume median diameters ranging from around 90 μm–210 μm. Sorption and energy storage properties were studied with STA.

The novel phase inversion method required as little as 2% weight silica for encapsulation. Sorption properties were evaluated under various temperatures and vapor pressures. Gravimetric energy storage densities under hydration conditions of $p_{H_2O} = 1.3$ kPa and $T = 30$ °C were in some cases over 97% of that of pure $CaCl_2$, suggesting that the silica nanoparticles in the shell have little effect on reaction enthalpies of encapsulated $CaCl_2$. However, in hydration conditions under which a solid tetrahydrate or hexahydrate was expected to appear, a liquid supersaturated solution seemed to form instead. This is likely due to the dihydrate undergoing deliquescence before the formation of a higher hydrate had time to develop.

Compositions with larger average capsule size generally showed decreased dehydration kinetics while increased silica content, which was found to lead to smaller capsules, ensured faster dehydration kinetics. However, in some cases a wide particle size distribution and resulting relatively high share of large capsules was more important factor in limiting reaction kinetics than average capsule size.

The direct mixing method, which produced capsules with higher spread in capsule size, showed decreased dehydration kinetics compared to the phase inversion method. However, as the solution concentration during preparation was also found to affect dehydration and hydration kinetics, the relationship between kinetics and preparation conditions seems to be rather complex and should be investigated further.

None of the tested samples, which contained approximately 5 mg of dry $CaCl_2$, showed signs of degradation in sorption properties under ten dehydration-hydration cycles performed under conditions in which samples went through complete deliquescence during hydration. Furthermore, the composition with the lowest amount of silica (2 wt%) showed no signs of degradation under 30 cycles. This suggests that the compositions are stable when used as a sorption TCES material.

Volumetric energy storage densities were predicted for a wide range of different hydration conditions based on the STA results. The results showed that volumetric energy storage density of up to 1.4 GJ/m^3 is achievable on bulk material level, without considering other system components, with temperature lifts as high as 30 °C. Such high values easily exceeding 1 GJ/m^3 are unprecedented in sorption TCES. Further optimization of the material could in best-case scenario yield volumetric energy storage densities of over 1.6 GJ/m^3 under similar conditions and with lower temperature lift of 20 °C, values close to 1.8 GJ/m^3 might be achievable. Thus, hydrophobic fumed silica encapsulation of $CaCl_2$, especially with the phase inversion method, shows excellent potential for seasonal thermal energy storage. However, larger scale experiments are still needed to prove the materials durability for practical applications.

CRediT authorship contribution statement

Aleksi Barsk: Writing – review & editing, Writing – original draft, Visualization, Validation, Methodology, Investigation, Funding acquisition, Formal analysis, Data curation, Conceptualization. **Maryam Roza Yazdani:** Writing – review & editing, Supervision, Methodology, Investigation, Formal analysis. **Ari Kankkunen:** Methodology, Investigation, Formal analysis. **Ari Seppälä:** Writing – review & editing, Supervision, Resources, Project administration, Conceptualization.

Declaration of competing interest

The authors declare that they have no known competing financial interests or personal relationships that could have appeared to influence the work reported in this paper.

Data availability

Data will be made available on request.

Acknowledgements

This work was supported by Finnish Cultural Foundation and Future Makers 2019 Program (funded by Technology Industries of Finland Centennial Foundation and Jane and Aatos Erkko Foundation). M.R.Y was funded by the Academy of Finland (343192). The research made use of OtaNano Nanomicroscopy Center (NMC). We also wish to thank Evonik for supplying the Aerosil fumed silica.

The authors wish to thank Prof. Annukka Santasalo-Aarnio and M. Sc. Konsta Turunen for their valuable comments.

Appendix A. Supplementary data

Supplementary data to this article can be found online at https://doi.org/10.1016/j.solmat.2022.112154.

References

[1] H. Mahon, D. O'Connor, D. Friedrich, B. Hughes, A review of thermal energy storage technologies for seasonal loops, Energy 239 (2022), 122207, https://doi.org/10.1016/J.ENERGY.2021.122207.

[2] J. Cot-Gores, A. Castell, L.F. Cabeza, Thermochemical energy storage and conversion: a-state-of-the-art review of the experimental research under practical conditions, Renew. Sustain. Energy Rev. 16 (2012) 5207–5224, https://doi.org/10.1016/J.RSER.2012.04.007.

[3] N. Yu, R.Z. Wang, L.W. Wang, Sorption thermal storage for solar energy, Prog. Energy Combust. Sci. 39 (2013) 489–514, https://doi.org/10.1016/J.PECS.2013.05.004.

[4] P.A.J. Donkers, L.C. Sögütoglu, H.P. Huinink, H.R. Fischer, O.C.G. Adan, A review of salt hydrates for seasonal heat storage in domestic applications, Appl. Energy 199 (2017) 45–68, https://doi.org/10.1016/J.APENERGY.2017.04.080.

[5] W. Li, J.J. Klemeš, Q. Wang, M. Zeng, Salt hydrate–based gas-solid thermochemical energy storage: current progress, challenges, and perspectives, Renew. Sustain. Energy Rev. 154 (2022), 111846, https://doi.org/10.1016/J.RSER.2021.111846.

[6] A. Shkatulov, R. Joosten, H. Fischer, H. Huinink, Core – shell encapsulation of salt hydrates into mesoporous silica shells for thermochemical energy storage, ACS Appl. Energy Mater. 3 (2020) 6860–6869, https://doi.org/10.1021/acsaem.0c00971.

[7] Y. Yuan, H. Zhang, F. Yang, N. Zhang, X. Cao, Inorganic composite sorbents for water vapor sorption: a research progress, Renew. Sustain. Energy Rev. 54 (2016) 761–776, https://doi.org/10.1016/J.RSER.2015.10.069.

[8] T.S. Yan, T.X. Li, J.X. Xu, J.W. Chao, Understanding the transition process of phase change and dehydration reaction of salt hydrate for thermal energy storage, Appl. Therm. Eng. 166 (2020), 114655, https://doi.org/10.1016/J.APPLTHERMALENG.2019.114655.

[9] R.J. Clark, A. Mehrabadi, M. Farid, State of the art on salt hydrate thermochemical energy storage systems for use in building applications, J. Energy Storage 27 (2020), 101145, https://doi.org/10.1016/J.EST.2019.101145.

[10] V. Palomba, A. Frazzica, Recent advancements in sorption technology for solar thermal energy storage applications, Sol. Energy 192 (2019) 69–105, https://doi.org/10.1016/J.SOLENER.2018.06.102.

[11] M. Gaeini, A.L. Rouws, J.W.O. Salari, H.A. Zondag, C.C.M. Rindt, Characterization of microencapsulated and impregnated porous host materials based on calcium chloride for thermochemical energy storage, Appl. Energy 212 (2018) 1165–1177, https://doi.org/10.1016/j.apenergy.2017.12.131.

[12] B.G.P. Van Ravensteijn, P.A.J. Donkers, R.C. Ruliaman, J. Eversdijk, H.R. Fischer, H.P. Huinink, O.C.G. Adan, B.G.P. van Ravensteijn, P.A.J. Donkers, R.C. Ruliaman, J. Eversdijk, H.R. Fischer, H.P. Huinink, O.C.G. Adan, Encapsulation of salt hydrates by polymer coatings for low-temperature heat storage applications, ACS Appl. Polym. Mater. 3 (2021) 1712–1726, https://doi.org/10.1021/acsapm.0c01186.

[13] B.P. Binks, R. Murakami, Phase inversion of particle-stabilized materials from foams to dry water, Nat. Mater. 511 (5) (2006) 865–869, https://doi.org/10.1038/nmat1757, 2006.

[14] R. Dawson, L.A. Stevens, O.S.A. Williams, W. Wang, B.O. Carter, S. Sutton, T. C. Drage, F. Blanc, D.J. Adams, A.I. Cooper, 'Dry bases': carbon dioxide capture using alkaline dry water, Energy Environ. Sci. 7 (2014) 1786–1791, https://doi.org/10.1039/C3EE44124E.

[15] L. Forny, I. Pezron, K. Saleh, P. Guigon, L. Komunjer, Storing water in powder form by self-assembling hydrophobic silica nanoparticles, Powder Technol. 171 (2007) 15–24, https://doi.org/10.1016/J.POWTEC.2006.09.006.

[16] L. Forny, K. Saleh, R. Denoyel, I. Pezron, Contact angle assessment of hydrophobic silica nanoparticles related to the mechanisms of dry water formation, Langmuir 26 (2009) 2333–2338, https://doi.org/10.1021/LA902759S.

[17] K. Saleh, L. Forny, P. Guigon, I. Pezron, Dry water: from physico-chemical aspects to process-related parameters, Chem. Eng. Res. Des. 89 (2011) 537–544, https://doi.org/10.1016/J.CHERD.2010.06.005.

[18] M. Al-Wabel, J. Elfaki, A. Usman, Q. Hussain, Y.S. Ok, Performance of dry water- and porous carbon-based sorbents for carbon dioxide capture, Environ. Res. 174 (2019) 69–79, https://doi.org/10.1016/J.ENVRES.2019.04.020.

[19] X. Rong, H. Yang, N. Zhao, Rationally turning the interface activity of mesoporous silicas for preparing pickering foam and "dry water", Langmuir 33 (2017) 9025–9033, https://doi.org/10.1021/acs.langmuir.7b01702.

[20] L. Sun, S. Wang, Z. Liu, A.T. Smith, Y. Zeng, L. Sun, W. Wang, Dry hydrated potassium carbonate for effective CO 2 capture, Dalton Trans. 49 (2020) 3965–3969, https://doi.org/10.1039/C9DT01909J.

[21] G. Bolin, D. Glebov, Salt coated with nanoparticles, United States Patent US 9 (2016) 459, 026 B2.

[22] Aerosil Evonik, Fumed Silica: Technical Overview, 2015. https://products.evonik.com/assets/45/92/244592.pdf.

[23] B.P. Binks, A.J. Johnson, J.A. Rodrigues, Inversion of 'dry water' to aqueous foam on addition of surfactant, Soft Matter 6 (2009) 126–135, https://doi.org/10.1039/B914706C.

[24] M.R. Conde, Properties of aqueous solutions of lithium and calcium chlorides: formulations for use in air conditioning equipment design, Int. J. Therm. Sci. 43 (2004) 367–382, https://doi.org/10.1016/J.IJTHERMALSCI.2003.09.003.

[25] K.K. Meisingset, F. Grønvold, Thermodynamic properties and phase transitions of salt hydrates between 270 and 400 K IV. CaCl2·6H2O, CaCl2·4H2O, CaCl2·2H2O, and FeCl3·6H2O, J. Chem. Thermodyn. 18 (1986) 159–173, https://doi.org/10.1016/0021-9614(86)90130-8.

[26] K.S. Pitzer, C.S. Oakes, Thermodynamics of calcium chloride in concentrated aqueous solutions and in crystals, J. Chem. Eng. Data 39 (1994) 553–559, https://doi.org/10.1021/je00015a035.

[27] K.K. Kelley, G.E. Moore, The specific heats at low temperatures of anhydrous chlorides of calcium, iron, magnesium and manganese, J. Am. Chem. Soc. 65 (1943) 1264–1267, https://doi.org/10.1021/ja01247a003.

[28] M. Molenda, J. Stengler, M. Linder, A. Wörner, Reversible hydration behavior of CaCl2 at high H2O partial pressures for thermochemical energy storage, Thermochim. Acta 560 (2013) 76–81, https://doi.org/10.1016/J.TCA.2013.03.020.

[29] A.B. Subramaniam, M. Abkarian, L. Mahadevan, H.A. Stone, Non-spherical bubbles, 2005 4387070, Nature 438 (2005), https://doi.org/10.1038/438930a, 930–930.

[30] Z. Liu, X. Fu, B.P. Binks, H.C. Shum, Mechanical compression to characterize the robustness of liquid marbles, Langmuir 31 (2015) 11236–11242, https://doi.org/10.1021/acs.langmuir.5b02792.

[31] A. Lannung, Dampfdruckmessungen des Systems Calciumchlorid–Wasser, Z. Anorg. Allg. Chem. 228 (1936) 1–18, https://doi.org/10.1002/zaac.19362280102.

[32] R.V. Gough, V.F. Chevrier, M.A. Tolbert, Formation of liquid water at low temperatures via the deliquescence of calcium chloride: implications for Antarctica and Mars, Planet, Space Sci 131 (2016) 79–87, https://doi.org/10.1016/J.PSS.2016.07.006.

[33] L. Guo, W. Gu, C. Peng, W. Wang, Y.J. Li, T. Zong, Y. Tang, Z. Wu, Q. Lin, M. Ge, G. Zhang, M. Hu, X. Bi, X. Wang, M. Tang, A comprehensive study of hygroscopic properties of calcium- and magnesium-containing salts: implication for hygroscopicity of mineral dust and sea salt aerosols, Atmos. Chem. Phys. 19 (2019) 2115–2133, https://doi.org/10.5194/acp-19-2115-2019.

[34] J.T. Kelly, A.S. Wexler, Thermodynamics of carbonates and hydrates related to heterogeneous reactions involving mineral aerosol, J. Geophys. Res. Atmos. 110 (2005) 1–13, https://doi.org/10.1029/2004JD005583.

[35] A. Permyakova, S. Wang, E. Courbon, F. Nouar, N. Heymans, P. D'Ans, N. Barrier, P. Billemont, G. De Weireld, N. Steunou, M. Frère, C. Serre, Design of salt–metal organic framework composites for seasonal heat storage applications, J. Mater. Chem. A. 5 (2017) 12889–12898, https://doi.org/10.1039/C7TA03069J.

[36] E. Courbon, P. D'Ans, A. Permyakova, O. Skrylnyk, N. Steunou, M. Degrez, M. Frère, Further improvement of the synthesis of silica gel and CaCl2 composites: enhancement of energy storage density and stability over cycles for solar heat storage coupled with space heating applications, Sol. Energy 157 (2017) 532–541, https://doi.org/10.1016/J.SOLENER.2017.08.034.

[37] W. Li, J.J. Klemeš, Q. Wang, M. Zeng, Characterisation and sorption behaviour of LiOH-LiCl@EG composite sorbents for thermochemical energy storage with controllable thermal upgradeability, Chem. Eng. J. 421 (2021), 129586, https://doi.org/10.1016/J.CEJ.2021.129586.

[38] A.I. Shkatulov, J. Houben, H. Fischer, H.P. Huinink, Stabilization of K2CO3 in vermiculite for thermochemical energy storage, Renew. Energy 150 (2020) 990–1000, https://doi.org/10.1016/J.RENENE.2019.11.119.

[39] J.X. Xu, T.X. Li, J.W. Chao, T.S. Yan, R.Z. Wang, High energy-density multi-form thermochemical energy storage based on multi-step sorption processes, Energy 185 (2019) 1131–1142, https://doi.org/10.1016/J.ENERGY.2019.07.076.